NANOPARTICLES

Octahedral palladium nanoparticles as excellent hosts for electrochemically adsorbed and absorbed hydrogen

Anna Zalineeva,[1] Stève Baranton,[1]* Christophe Coutanceau,[1] Gregory Jerkiewicz[2]*

We report new results for electrochemical H adsorption on and absorption in octahedral palladium nanoparticles (Pd-NPs) with an average tip-to-tip size of 7.8 nm and a narrow size distribution. They reveal a very high H loading of 0.90 that cannot be achieved using bulk Pd materials or larger NPs; this behavior is assigned to a combination of two factors: their small size and face morphology. Temperature-dependent cyclic voltammetry (CV) studies in the range of 296 to 333 K reveal unique features that are attributed to electrochemical H adsorption, H absorption, and H_2 generation. The CV features are used to prepare H adsorption and absorption isotherms that are then used in thermodynamic data analysis. Modeling of the experimental results demonstrates that, upon H adsorption and absorption, Pd-NPs develop a core-shell-skin structure, each with its unique H loading. The electrochemical results obtained for octahedral Pd-NPs are compared to analogous data obtained for cubic Pd-NPs with a similar size as well as for larger cubic Pd-NPs and bulk materials under gas-phase conditions.

INTRODUCTION

Palladium (Pd) in the form of preferentially shaped nanoparticles (NPs) or thin layers is an excellent catalyst that finds application in a wide range of chemical reactions (1–3), and its cost makes it an attractive alternative to platinum (Pt)–based materials. Nanoparticles have a significant value of dispersion (the fraction of atoms of a material belonging to its surface), as compared to bulk materials whose dispersion values are practically zero; thus, they offer effective utilization of expensive or rare materials that have excellent catalytic properties. Pd is an excellent hydrogen (H) host and serves as a model system in research on H absorption and desorption (4). Non-noble intermetallic materials of AB_5 and AB_2 types are also excellent H hosts (5, 6) and find application as anodes in rechargeable nickel–metal hydride [Ni-M(H)] batteries (7). The charge and discharge kinetics of Ni-M(H) batteries are limited by the slow H diffusion in solids. This kinetic limitation can be overcome through the use of NPs that, due to their dimensions, can be quickly loaded with H. In addition, NPs offer natural resilience to pulverization and stable H storage capacity upon repetitive charge-discharge cycling. Pd is capable of both adsorbing and absorbing H, and, in the case of bulk materials, the amount of adsorbed H (H_{ads}) is tiny as compared to the amount of absorbed H (H_{abs}). H adsorption and absorption can be accomplished under gas-phase and electrochemical conditions, but the respective mechanisms are different owing to the nature of the H precursor (8–10). At the ambient temperature (T), H absorption under gas-phase conditions requires elevated pressures (p); the higher the pressure, the greater the amount of H_{abs}. Under electrochemical conditions, H absorption is accomplished by applying a potential (E) at which the electrolytic H_2 generation takes place (H_2 generation and H absorption occur concurrently) and the amount of H_{abs} can be related to the value of E. Pt group metals (PGMs) reveal a unique ability to adsorb H at positive overpotentials (η) with respect to the onset potential of the hydrogen evolution reaction (HER); this process is called the underpotential deposition of H (UPD H), and the species is called the underpotential deposited H (H_{UPD}). The adsorption of H intermediate involved in the H_2 generation at negative η is called the

overpotential deposition of H (OPD H), and the species is called the overpotential deposited H (H_{OPD}) (8). In the case of bulk Pd, the efficiency of H absorption in the UPD H region is 100% because it is not accompanied by any other faradaic process. On the other hand, the efficiency of H absorption in the OPD H range is lower due to the concurrent H_2 generation (9). Because UPD H is accompanied by H absorption, it is impossible to determine the surface coverage (θ) of H_{UPD} and to examine thermodynamics of the process, unlike in the case of Pt materials (8, 10). Pd nanomaterials reveal higher H loading than do bulk materials (11–13), and suitable electrochemical conditions result in the separation of cyclic voltammetry (CV) features assigned to UPD H, H absorption, and HER (14).

Here, we report on the preparation of small octahedral and cubic Pd-NPs with an average size of 7.8 and 10 nm, respectively, and a narrow size distribution, followed by their application in temperature-dependent electrochemical research. An electron microscopy analysis demonstrates that these Pd-NPs maintain their shape and size after repetitive potential cycling, thus maintaining structural integrity. Then, we conduct temperature-dependent electrochemical measurements to study H adsorption on and absorption in these Pd-NPs and to analyze the energetics of these processes. The thermodynamic data are compared to analogous results obtained for bulk Pd materials to identify phenomena originating from the nanoscopic size and surface morphology of the Pd particles. This comparative analysis reveals that the octahedral Pd-NPs absorb remarkably more H than do the cubic Pd-NPs of similar size, larger NPs, or bulk Pd materials. We model the electrochemical H adsorption and absorption data to determine whether the Pd-NPs develop an inner structure that is unique to their size and observe a core-shell-skin structure. Last, we discuss that the high H loading makes the octahedral Pd-NPs very promising materials for applications such as H storage and metal hydride batteries.

RESULTS

Electrochemical H adsorption on and absorption in octahedral Pd-NPs

Figure 1A presents a high-resolution transmission electron microscopy (HR-TEM) image of octahedral Pd-NPs placed on a carbon membrane that serves as a substrate. The inset shows an image of a single NP and the corresponding fast Fourier transform (FFT) pattern. It reveals that the octahedral NPs are truncated at the extreme ends, and the FFT pattern

[1]Institut de Chimie des Milieux et Matériaux de Poitiers (IC2MP), UMR CNRS 7285, Equipe "Catalyse et Milieux Non Conventionnels," Université de Poitiers, 4 rue Michel Brunet, TSA 51106, 86073 Poitiers Cedex 9, France. [2]Department of Chemistry, Queen's University, 90 Bader Lane, Kingston, Ontario K7L 3N6, Canada.
*Corresponding author. Email: steve.baranton@univ-poitiers.fr (S.B.); gregory.jerkiewicz@chem.queensu.ca (G.J.)
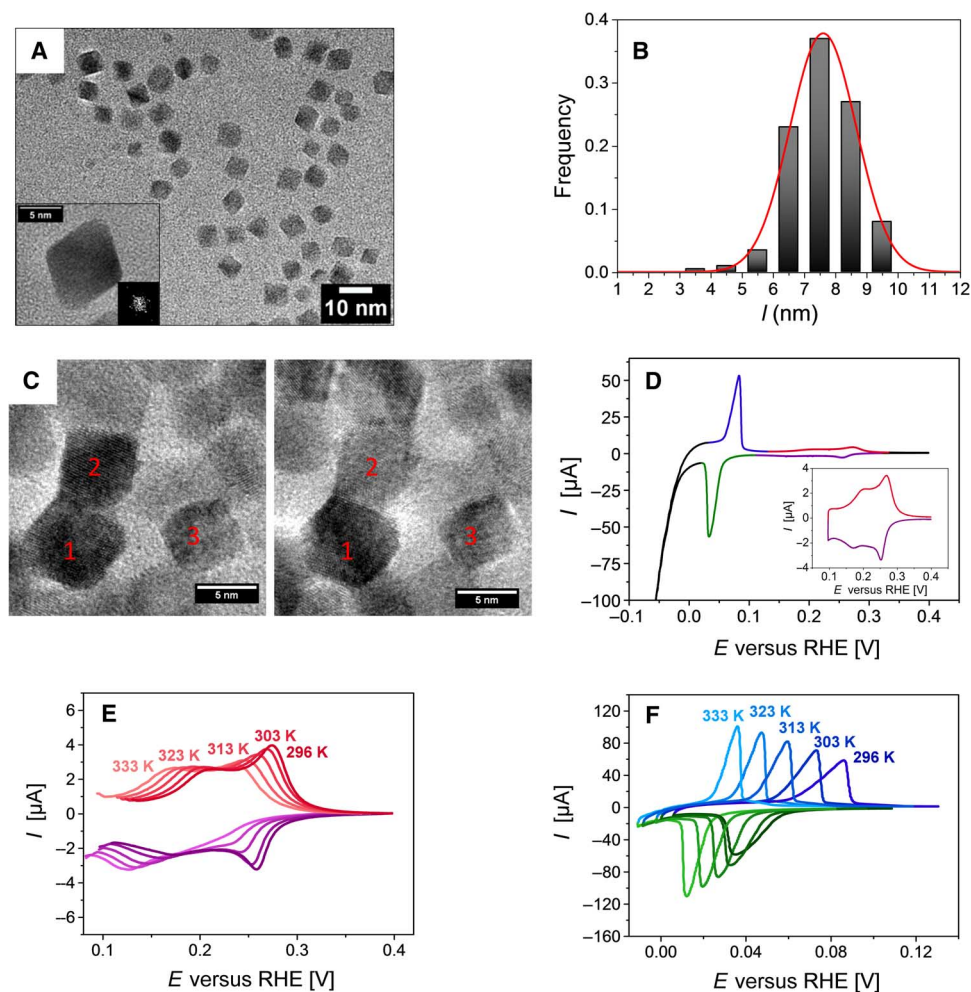
Fig. 1. Physical and electrochemical characterization of octahedral Pd-NPs. (**A**) HR-TEM image of octahedral Pd-NPs. The inset shows an image of a single NP and the corresponding FFT pattern. (**B**) Histogram showing the NP size (l) distribution. (**C**) IL-TEM images of the octahedral Pd-NPs before and after potential cycling in the range of 0 to 0.40 V. (**D**) CV profile for octahedral Pd-NPs acquired in 0.5 M aqueous H_2SO_4 solution at $T = 296$ K and $s = 1.0$ mV s^{-1} in the range of −0.05 to 0.40 V. The purple and red transients refer to UPD H (shown in detail in the inset), the green and blue transients refer to H absorption and H_{abs} desorption, and the black transient refers to HER. RHE, reversible hydrogen electrode. (**E**) CV profiles for H_{UPD} adsorption (shades of purple) and desorption (shades of red), and (**F**) CV profiles for H absorption (shades of green) and H_{abs} desorption (shades of blue) for five temperature values acquired in 0.5 M aqueous H_2SO_4 solution at $s = 1.0$ mV s^{-1}.

shows that the NPs are crystalline in nature. The main image is used to determine the length (l) of the octahedral NPs, which refers to the tip-to-tip distance. Figure 1B presents a histogram showing that the values of l fall in the range of 6 to 9 nm, with an average size of 7.8 nm, which corresponds to an average edge length of 5.5 nm. Figure 1C presents identical location TEM (IL-TEM) images of the octahedral Pd-NPs before and after potential cycling in the regions of UPD H and H absorption and H_{abs} desorption in the range of 0 to 0.40 V. A comparative analysis of the IL-TEM images reveals that the NPs maintain the same shape and size even after 10 potential transients. The stability of Pd-NPs in this potential range is not surprising because the standard potentials of the Pd^{2+}(aq)/Pd(s) and PdO(s),H^+(aq)/Pd(s),H_2O(l) redox couples are 0.95 and 0.79 V, respectively (*15*). In addition, cubic Pd-NPs that were prepared using the same procedure as described here were cycled 100 times in a similar potential range. IL-TEM measurements demonstrated that they maintained their initial size and shape (*16*). The brightness of some NPs slightly changes because of a small shift of the carbon

membrane, which gives rise to a change in the focal length. However, the location and relative distance between the three main NPs (1 to 3) remain unaltered. The lack of any structural or dimensional changes in Pd-NPs suggests that the NPs do not undergo chemical or electro-chemical dissolution upon potential cycling in the range of 0 to 0.40 V. In addition, the NPs do not undergo pulverization or any other structural change that could be caused by H absorption and H_{abs} desorption. It is an important observation, which stipulates that pulverization of inter-metallic H hosts is due to the presence of grain boundaries and other structural defects that NPs do not have. Figure 1D presents a CV profile for the octahedral Pd-NPs acquired in 0.5 M aqueous H_2SO_4 solution at a temperature of $T = 296$ K and a potential scan rate of $s = 1.0$ mV s^{-1}, with the lower and upper potential limits of −0.05 and 0.40 V, respectively. It is color-coded to emphasize the cathodic and anodic ranges corresponding to different electrochemical processes involving H. The asymmetric features in the range of 0.12 to 0.30 V are associated with H_{UPD} adsorption (purple) and desorption (red). Because, at $s = 1.0$ mV s^{-1}, the current

associated with these processes is small, it is shown on a different scale in the inset. The well-defined but asymmetric cathodic (green) and anodic (blue) peaks in the range of 0 to 0.12 V are due to H absorption and desorption of H_{abs}, whereas the gradually increasing current (I) at $E <$ −0.025 V (black) is due to the electrolytic H_2 generation occurring on the surfaces of octahedral Pd-NPs now modified by H_{UPD} and H_{abs}. The separation of CV characteristics associated with these processes is a unique feature related to the nanoscopic size of the particles because this effect is not observed in the case of bulk Pd materials ([17], [18]). Figure 1E presents a set of CV profiles for H_{UPD} adsorption (shades of purple) and desorption (shades of red) for temperatures in the range of $296 \leq T \leq 333$ K acquired in 0.5 M aqueous H_2SO_4 solution at $s =$ 1.0 mV s^{-1}. The temperature increase shifts all the features toward lower potentials and slightly modifies their shapes. The cathodic and anodic charges are the same, and their integration (allowing for the double-layer charging) yields the charge (Q) values that are $Q = 400 \pm$ 12 μC for the entire temperature range, indicating that the amount of adsorbed and desorbed H_{UPD} is unaffected by T modification. Figure 1F presents a set of CV profiles for H absorption (shades of green) and H_{abs} desorption (shades of blue) at the same condition, as specified above. The temperature increase shifts the cathodic and anodic peaks toward lower potentials and makes the peaks sharper. Integration of the cathodic and anodic peaks (allowing for the double-layer charging) yields the values of Q associated with H absorption and desorption of H_{abs}. For the entire temperature range, the value is consistently $Q = 1240 \pm$ 50 μC, implying that the amount of H_{abs} is unaffected by T modification. In addition, the amount of absorbed H equals the amount of desorbed H_{abs}, indicating that there is no residual H_{abs} remaining in the lattice of octahedral Pd-NPs. Consequently, their charge and discharge capacities are the same. The absence of changes in the CV profiles indicates that not only the octahedral Pd-NPs maintain their size but also the NP facets do not undergo reconstruction or restructuring. For comparative analysis, we performed analogous experiments using cubic Pd-NPs with an average size of 10 nm. Figure S1 presents the following results: an HR-TEM image for cubic Pd-NPs (fig. S1A), a CV profile in the range of −0.05 to 0.40 V at $T = 293$ K (fig. S1B), a series of CV profiles for H_{UPD} adsorption and desorption at four different temperature values (fig. S1C), and a series of CV profiles for H absorption and H_{abs} desorption at five different temperature values (fig. S1D). The series of CV profiles were acquired in 0.5 M aqueous H_2SO_4 at $s =$ 1.0 mV s^{-1}. The charge associated with H_{UPD} adsorption and desorption is $Q = 291 \pm 11$ μC, and the charge due to H absorption and H_{abs} desorption is $Q = 2060 \pm 84$ μC for the entire temperature range. As in the case of octahedral Pt-NPs, the temperature variation does not affect the amount of adsorbed or absorbed H. In a subsequent section, these CV profiles are used to prepare adsorption, absorption, and desorption isotherms that then serve in thermodynamic analyses of these processes.
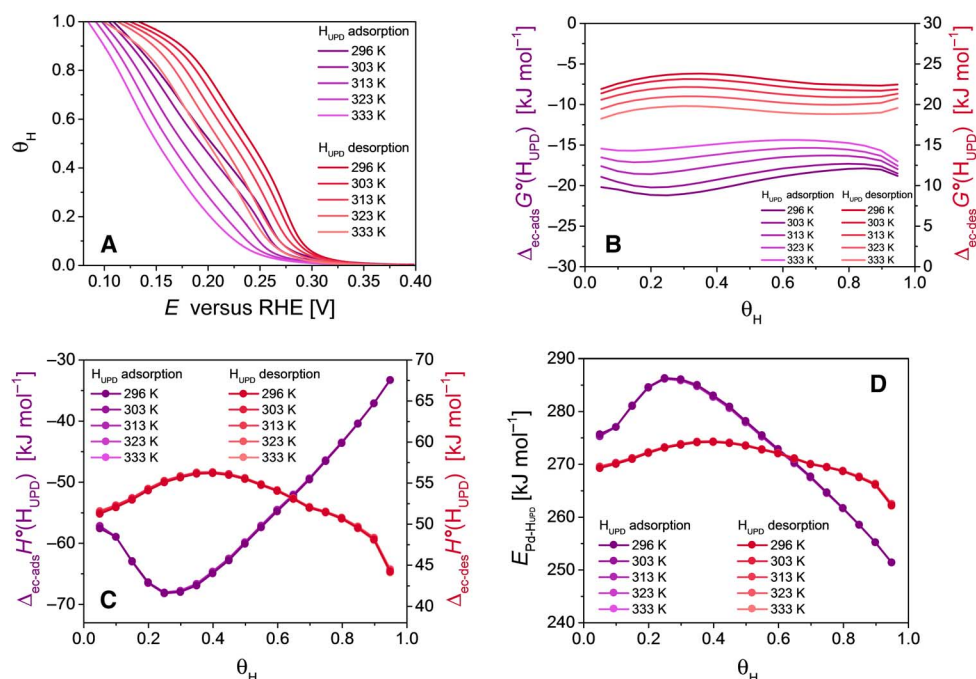
Thermodynamics of electrochemical H adsorption

Figure 2A presents isotherms for adsorption and desorption of H_{UPD} on the octahedral Pd-NPs at temperatures in the range of $296 \leq T \leq$ 333 K, which are prepared on the basis of the CV profiles shown in Fig. 1E. Because the H_{UPD} adsorption and desorption CV profiles are not mirror images, the adsorption and desorption isotherms do not overlap, generating a hysteresis, the origin of which is discussed later. The data demonstrate that to maintain a given H_{UPD} surface coverage (θ_H) while increasing the temperature, the applied potential has to be decreased. Because the H_{UPD} adsorption (cathodic) CV profile is asymmetric

and the current (I) drops steeply as E approaches the onset of H_2 generation, the adsorption isotherms are not S-shaped; a similar behavior is observed for the H_{UPD} desorption isotherm. The application of the general electrochemical adsorption isotherm (Eq. 1) allows the determination of the standard Gibbs energy of H_{UPD} electrochemical adsorption and desorption [$\Delta_{ec-ads}G°(H_{UPD})$ and $\Delta_{ec-des}G°(H_{UPD})$] as a function of θ_H and T ([19])

$$\frac{\theta_{H_{UPD}}}{1 - \theta_{H_{UPD}}} = \sqrt{f_{H_2}} \, \exp\left(\frac{-E_{RHE}F}{RT}\right) \, \exp\left(\frac{-\Delta_{ec-ads}G°(H_{UPD})}{RT}\right) \quad (1)$$

where f_{H_2} ($f_{H_2} = 1$ bar) is the fugacity of $H_2(g)$ in the reference electrode compartment and E_{RHE} is the potential measured with respect to RHE. Figure 2B presents graphs of $\Delta_{ec-ads}G°(H_{UPD})$ and $\Delta_{ec-des}G°(H_{UPD})$ as a function of θ_H for the temperatures studied. These relationships are wave-shaped and show that the values of $\Delta_{ec-ads}G°(H_{UPD})$ vary between −21.3 and −14.4 kJ mol^{-1} and those of $\Delta_{ec-des}G°(H_{UPD})$ vary between +18.7 and +23.8 kJ mol^{-1}. For every θ_H, the value of $\Delta_{ec-ads}G°(H_{UPD})$ becomes less negative and that of $\Delta_{ec-des}G°(H_{UPD})$ becomes less positive as T increases. This behavior arises directly from the changes in the CV profiles brought about by T increase (Fig. 1E), that is, progressively lower potentials have to be applied as temperature increases to achieve the same values of θ_H (Fig. 2A). Because the H_{UPD} adsorption and desorption CV profiles are not mirror images, for a given T, the absolute values of $\Delta_{ec-ads}G°(H_{UPD})$ and $\Delta_{ec-des}G°(H_{UPD})$ are different. This behavior is unique to Pd-NPs because, in the case of Pt(111) and even Pt(poly) electrodes as well as Pt-NPs, the respective CV profiles are almost mirror images ([8], [10], [20], [21]). Because for every pair of T and θ_H values the absolute value of $\Delta_{ec-des}G°(H_{UPD})$ is greater than that of $\Delta_{ec-ads}G°(H_{UPD})$, their sum $\delta\Delta G°(H_{UPD}) = \Delta_{ec-ads}G°(H_{UPD}) + \Delta_{ec-des}G°(H_{UPD})$ always adopts positive values between +1.5 and +4.5 kJ mol^{-1} (see fig. S2).

It is important to analyze the origin of the asymmetry in the CV profiles for H_{UPD} adsorption and desorption. Because the potential scan rate is very low ($s = 1.0$ mV s^{-1}), we propose that the asymmetry in the CV profiles arises for nonkinetic reasons and has a thermodynamic origin. A complete CV profile refers to a close thermodynamic cycle, meaning $\oint \Delta G° = 0$. The nonzero $\delta\Delta G°(H_{UPD})$ might be attributed to one or more concurrently occurring interfacial processes, such as reconstruction of nanocrystalline facets ($\Delta_{reconst}G°$), NP compression ($\Delta_{compr}G°$), changes in interfacial hydration ($\Delta_{hydr}G°$), or NP dissolution ($\Delta_{dissol}G°$). The reconstruction of nanocrystalline facets can be excluded (thus, $\Delta_{reconst}G° = 0$) because the CV profiles do not undergo any changes for all temperatures used, and the IL-TEM images (Fig. 1C) reveal that the octahedral Pd-NPs preserve their shape and size. The IL-TEM measurements also imply that there is no dissolution of Pd-NPs; thus, $\Delta_{dissol}G° = 0$. This behavior is expected because the standard potentials of the $Pd^{2+}(aq)/Pd(s)$ and $PdO(s),H^{+}(aq)/Pd(s),H_2O(l)$ redox couples are 0.95 and 0.79 V, respectively, and the highest potential applied in this study is 0.40 V ([15]). Compression is not expected to play a significant role in the H_{UPD} thermodynamics (thus, $\Delta_{compr}G° = 0$) because the process is limited to the topmost substrate layers and does not involve the entire three-dimensional structure of Pd-NPs. Having excluded these three phenomena, we propose that the nonzero value of $\delta\Delta G°(H_{UPD})$ is due to changes in the interfacial interactions of the electrolyte components (hydrated cations and H_2O molecules) with Pd-NPs. This proposal is supported by the observation that noncovalent interactions

Fig. 2. Thermodynamical data for adsorption and desorption of H_{UPD} on octahedral Pd-NPs. (**A**) Adsorption and desorption isotherms for H_{UPD} on octahedral Pd-NPs at five temperatures in the range of $296 \leq T \leq 333$ K. (**B**) Plots of $\Delta_{ec\text{-}ads}G°(H_{UPD})$ and $\Delta_{ec\text{-}des}G°(H_{UPD})$ as a function of θ_H for the five temperature values. (**C**) Plots of $\Delta_{ec\text{-}ads}H°(H_{UPD})$ and $\Delta_{ec\text{-}des}H°(H_{UPD})$ as a function of θ_H for the five temperature values. (**D**) Plots of $E_{Pd-H_{UPD}}$ as a function of θ_H for the five temperature values.

between Pt materials and hydrated alkali cations [$Pt_{surface}$–$M^+(aq)$] were reported to affect kinetics of reactions occurring at Pt electrocatalysts in fuel cells by blocking active surface sites (*22*). Elsewhere (*23*, *24*), it was reported that the wetting ability of Pt materials undergoes a significant change upon the adsorption of H_{UPD}, making the surface hydrophobic-like and altering the strength of $Pt_{surface}$–H_2O interactions. Because the $Pt_{surface}$–$M^+(aq)$ and $Pt_{surface}$–H_2O interactions do not involve an external charge transfer that would give rise to a significant feature in CV transients, any change in their strength cannot be detected using this technique but can be detected indirectly through the nonzero value of $\delta G°(H_{UPD})$. The entire $\delta G°(H_{UPD})$ has two components, cathodic [$\delta\Delta_{cath}G°(H_{UPD})$] and anodic [$\delta\Delta_{anod}G°(H_{UPD})$], and $\delta G°(H_{UPD}) = \delta\Delta_{cath}G°(H_{UPD}) + \delta\Delta_{anod}G°(H_{UPD})$; $\delta G°(H_{UPD})$ accounts for the Gibbs energy changes associated with other phenomena (here, the interactions of the electrolyte components with Pd-NPs) occurring simultaneously with UPD H. The positive values of $\delta G°(H_{UPD})$ imply that, for all θ_H and T values, more Gibbs energy is supplied to the system upon H_{UPD} desorption than is released during its adsorption, as a consequence of the existence of two energetically different surface states (unmodified Pd and H_{UPD}-modified Pd surfaces). However, because a complete CV transient commencing and ending at 0.40 V corresponds to a closed thermodynamic cycle, the sum of all individual Gibbs energy contributions is equal to zero; thus, $\Delta_{ec\text{-}ads}G°(H_{UPD}) + \Delta_{ec\text{-}des}G°(H_{UPD}) + \delta\Delta_{cath}G°(H_{UPD}) + \delta\Delta_{anod}G°(H_{UPD}) = 0$.

For a given value of θ_H, the relationships between $\Delta_{ec\text{-}ads}G°(H_{UPD})$ and T or $\Delta_{ec\text{-}des}G°(H_{UPD})$ and T are linear (the correlation coefficient is 0.99), allowing the determination of the entropy of electrochemical H adsorption and desorption [$\Delta_{ec\text{-}ads}S°(H_{UPD})$ and $\Delta_{ec\text{-}des}S°(H_{UPD})$]; see fig. S3]; $\Delta_{ec\text{-}ads}S°(H_{UPD})$ is negative and $\Delta_{ec\text{-}des}S°(H_{UPD})$ is positive for the entire range of θ_H. In addition, these values are more negative and

more positive, respectively, than those for H_{UPD} adsorption on Pt(111), Pt(poly), and Rh(poly) electrodes (*8*, *10*, *19*). Although both Pt and Pd adopt the face-centered cubic (fcc) structure, the more negative values of $\Delta_{ec\text{-}ads}S°(H_{UPD})$ and the more positive values of $\Delta_{ec\text{-}des}S°(H_{UPD})$ for the octahedral Pd-NPs point to a higher degree of H_{UPD} immobilization (a stronger surface bond) in the Pd-NP lattice than in the case of bulk Pt and Rh that have practically infinite lattices. This behavior can be related to the lattice parameter of Pd-NPs that is slightly reduced (lattice contraction) as compared to bulk Pd (*25*). Thus, an embedded H_{UPD} adsorbed atom resides in a slightly tighter (compressed) metallic lattice of an NP as compared to the lattice of a bulk Pd material. It is important to add that we could not compare the behavior of Pd-NPs to that of bulk Pd materials because, as we explained in the Introduction, the electrochemical H adsorption (UPD H) cannot be examined using bulk materials because of the concurrently occurring H absorption and HER. In addition, there are no thermodynamic data for UPD H on Pt-NPs and, consequently, any quantitative analysis is limited to bulk Pt and Rh materials and Pd-NPs.

Knowledge of the values of $\Delta_{ec\text{-}ads}G°(H_{UPD})$, $\Delta_{ec\text{-}des}G°(H_{UPD})$, $\Delta_{ec\text{-}ads}S°(H_{UPD})$, and $\Delta_{ec\text{-}des}S°(H_{UPD})$ allows the determination of the enthalpy of electrochemical H adsorption and desorption [$\Delta_{ec\text{-}ads}H°(H_{UPD})$ and $\Delta_{ec\text{-}des}H°(H_{UPD})$] as a function of θ_H for the entire range of T (Fig. 2C). The plots of $\Delta_{ec\text{-}ads}H°(H_{UPD})$ and $\Delta_{ec\text{-}des}H°(H_{UPD})$ versus θ_H for the five T values practically overlap (they vary by less than 0.1 kJ mol^{-1}), demonstrating that, in the case of the octahedral Pd-NPs, the temperature does not affect these state functions. The values of $\Delta_{ec\text{-}ads}H°(H_{UPD})$ are between -68.2 and -33.3 kJ mol^{-1}, and those of $\Delta_{ec\text{-}des}H°(H_{UPD})$ are between $+44.0$ and $+56.3$ kJ mol^{-1}. In the case of $0.05 \leq \theta_H \leq 0.60$, $\delta\Delta H°(H_{UPD}) = \Delta_{ec\text{-}ads}H°(H_{UPD}) + \Delta_{ec\text{-}des}H°(H_{UPD})$ is negative, indicating that, for a given θ_H, more energy

in the form of heat is released during H_{UPD} adsorption than absorbed during its desorption. On the other hand, in the case of $0.65 \leq \theta_H \leq 0.95$, $\delta\Delta H°(H_{UPD})$ is positive, indicating that, for a given θ_H, less heat is released during H_{UPD} adsorption than absorbed during its desorption (fig. S4). A comparison of the values of $\Delta_{ec\text{-}ads}H°(H_{UPD})$ and $T \times \Delta_{ec\text{-}ads}S°(H_{UPD})$ shows that, for each T and the entire range of θ_H, $|\Delta_{ec-ads}H°(H_{UPD})| > |T \times \Delta_{ec\text{-}ads}S°(H_{UPD})|$; thus, UPD H on octahedral Pd-NPs is an enthalpy-driven process.

An analogous set of results for cubic Pd-NPs, namely, H_{UPD} adsorption and desorption isotherms, plots of $\Delta_{ec\text{-}ads}G°(H_{UPD})$, $\Delta_{ec\text{-}des}G°(H_{UPD})$, $\Delta_{ec\text{-}ads}H°(H_{UPD})$, and $\Delta_{ec\text{-}des}H°(H_{UPD})$ as a function of θ_H for the T values reported above are presented in fig. S5. The H_{UPD} adsorption and desorption isotherms have a slightly different shape that is attributed to the shape of NPs. The values of $\Delta_{ec\text{-}ads}G°(H_{UPD})$ vary between -21.4 and -14.8 kJ mol^{-1}, and those of $\Delta_{ec\text{-}des}G°(H_{UPD})$ vary between $+15.7$ and $+22.9$ kJ mol^{-1}. The values of $\Delta_{ec\text{-}ads}H°(H_{UPD})$ are between -54.7 and -40.5 kJ mol^{-1}, and those of $\Delta_{ec\text{-}des}H°(H_{UPD})$ are between $+42.1$ and $+58.3$ kJ mol^{-1}. A comparison of the results reveals that the magnitude of these thermodynamic state functions is similar for the two types of Pd-NPs.

Knowledge of the values of $\Delta_{ec\text{-}ads}H°(H_{UPD})$ and $\Delta_{ec\text{-}des}H°(H_{UPD})$ allows for the determination of the Pd–H_{UPD} surface bond energy ($E_{Pd-H_{UPD}}$) as a function of θ_H; the values of $E_{Pd-H_{UPD}}$ (Fig. 2D) depend only slightly on θ_H and vary between $+251$ and $+286$ kJ mol^{-1}. Similar results for cubic Pd-NPs are shown in fig. S5 and demonstrate that the respective $E_{Pd-H_{UPD}}$ values vary between $+259$ and $+276$ kJ mol^{-1}. The values of $E_{Pd-H_{UPD}}$ for the octahedral and cubic Pd-NPs are ca. 10% higher than analogous values for bulk Pt and Rh materials, both polycrystalline and single crystals (8, 10, 19). Although, at present, we are unaware of any surface bond energy values for H_{UPD} on Pt-NPs and our discussion is limited to Pd-NPs, we propose that the increase in the strength of Pd–H_{UPD} surface bond is due to the nanoscopic size of Pd octahedrons and contraction of the Pd-NP lattice, as compared to bulk Pd materials (25). In our earlier research (8, 10, 19), we indicated that the Pt–H_{UPD} and Rh–H_{UPD} surface bond energy values matched those for chemisorbed H (H_{chem}) under gas-phase conditions and, on the basis of thermodynamic analysis, concluded that these two species are equivalent and occupy the same surface adsorption sites, although the actual adsorption mechanisms are different in electrochemical and gas-phase environments (18). The actual adsorption site of H_{UPD} remains unknown, but it is accepted that it is strongly embedded in the fcc lattice of these metals and occupies either a multifold hollow site [threefold in the case of the (111) surface and fourfold in the case of the (100) surface] in the first surface layer or an octahedral site between the two topmost surface layers. The observation that very similar bond energies are observed for H_{UPD} residing on the surfaces of octahedral and cubic Pd-NPs and bulk Pt and Rh materials leads to the conclusion that, in the case of octahedral Pd-NPs, H_{UPD} occupies the same surface adsorption site as in the case of bulk materials. Because the Pd-NPs are octahedral and have predominantly (111) facets, we propose that H_{UPD} occupies either a threefold hollow site in the first surface layer or an octahedral site between the two topmost surface layers.

In the case of perfect octahedral Pd-NPs, all facets have the (111) orientation. Our TEM analysis indicates that the Pd-NPs are not perfect and lack two to three atomic layers at the corners and one to two atomic layers along the edges. Such modified corners and edges mimic the (100) and (110) structures, respectively. However, because they account for a tiny fraction of the overall surface area, their contribution to the overall electrochemical signals is negligible. Above, we determine thermo-

dynamic state functions for the electrochemical H adsorption on Pd-NPs and compare them to analogous data for bulk Pt and Pt(111) electrodes obtained also on the basis of temperature-dependent studies. At this stage of the discussion, it is important to add that there are no equivalent results for the Pt(100) or Pt(110) electrodes. Consequently, it is impossible to compare the thermodynamic data presented above to analogous results obtained for other Pt monocrystalline electrodes than Pt(111) or Pt(poly).

Thermodynamics of electrochemical H absorption

The temperature-dependent CV profiles (Fig. 1F) reveal well-defined features for H absorption and H_{abs} desorption. Because they do not overlap those assigned to UPD H or HER, they create a basis for the determination of H absorption and H_{abs} desorption isotherms as well as their thermodynamic analysis. Figure 3 (A and B) presents plots of H absorption and H_{abs} desorption isotherms expressed as E versus X_H and f_{H_2} versus X_H, where X_H is the lattice occupancy fraction defined as $X_H = N_H/N_{Pd,inn}$; N_H and $N_{Pd,inn}$ are the numbers of H_{abs} and inner Pd atoms per octahedral Pd-NP, respectively (see the Supplementary Materials). Because the surface Pd atoms participate in UPD H, only the inner atoms are involved in H absorption. The conversion of E values at which a given X_H is achieved to equivalent f_{H_2} values relates our findings to those for H absorption and H_{abs} desorption under gas-phase conditions (11). This conversion uses the Nernst equation and takes into account the mean activity coefficient of hydrated proton and other parameters (see the Supplementary Materials). The maximum H loading in octahedral Pd-NPs is found to be temperature-independent and corresponds to $X_H = 0.90$. The isotherms reveal a broad but sloped plateau as in the case of bulk materials and a hysteresis (4); the hysteresis implies that for given X_H and T, a higher value of f_{H_2} is required to drive H absorption than H_{abs} desorption. The plateau corresponds to the coexistence of the α and β phases and represents the transition from the α phase to the β phase during H absorption and from the β phase to the α phase during H_{abs} desorption. Elsewhere (26), it is reported that, in the case of single Pd-NPs, the plateau is practically horizontal, whereas it is sloped in the case of an ensemble of NPs. In our case, the sloped plateau is expected because we report results for an ensemble of Pd-NPs with a certain size distribution (see Fig. 1B). The E versus X_H and f_{H_2} versus X_H isotherms become practically vertical when X_H reaches 0.90, indicating that $X_H = 0.90$ corresponds to the maximum loading of H_{abs} and the application of even lower potentials (thus, higher equivalent f_{H_2} values) does not increase it any further. In fig. S6 (A and B), the graphs present E versus X_H and f_{H_2} versus X_H absorption and desorption isotherms prepared on the basis of the results shown in fig. S1. The results reveal that, in the case of cubic Pd-NPs, the maximum H loading is $X_H = 0.66$, thus substantially lower than in the case of the octahedral NPs. The isotherms reveal a broad but sloped plateau corresponding to the coexistence of the α and β phases. However, in the case of cubic Pd-NPs, significantly higher values of f_{H_2} are required to accomplish the same value of X_H (but still lower than 0.66), as in the case of octahedral Pd-NPs.

At this stage of the discussion, it is important to discuss the relationship between the potential of the H electrode and the H_2 fugacity (the effective H_2 pressure) as they appear in the Nernst equation for a specific activity of the hydrated H^+. The standard potential refers to the H_2 fugacity being equal to the standard pressure ($p° = 1$ bar) and the activity of H^+ being one. The Nernst equation represents an equilibrium between the H_2 fugacity above the electrolyte solution and the potential experienced by an electrode immersed in it. Positive potentials with
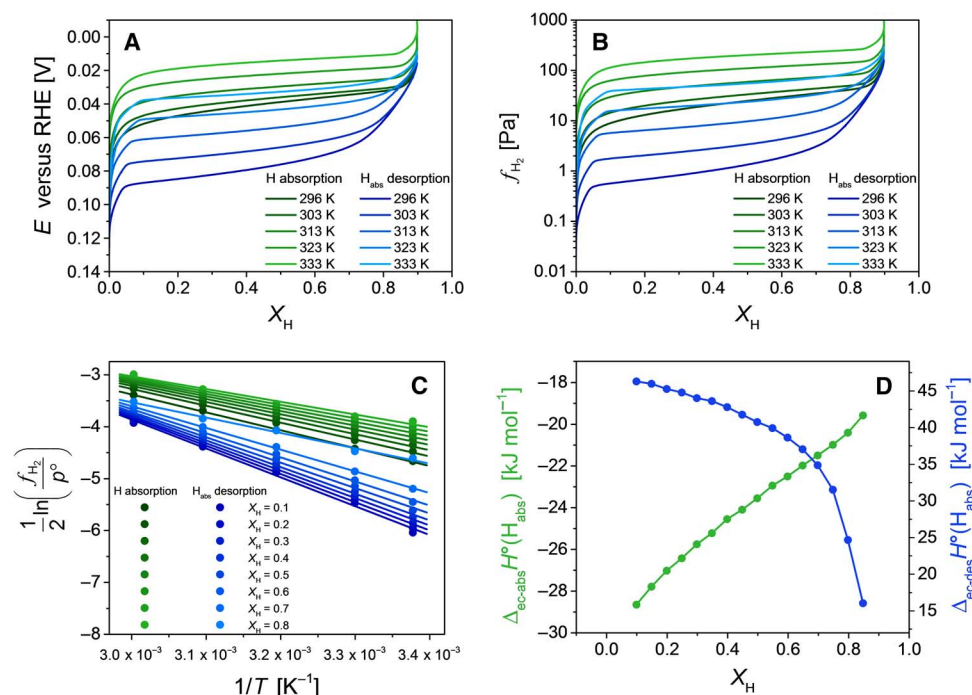
Fig. 3. Thermodynamical data for H absorption and H$_{abs}$ desorption in octahedral Pd-NPs. H absorption and H$_{abs}$ desorption isotherms expressed as E versus X_H (**A**) and f_{H_2} versus X_H (**B**) at five temperature values in the range of $296 \leq T \leq 333$ K. (**C**) van't Hoff plots of $\ln\left(\frac{f_{H_2}}{p^\circ}\right)$ versus $1/T$ for $0.10 \leq X_H \leq 0.80$. (**D**) Plots of $\Delta_{ec-abs}H^\circ(H_{abs})$ and $\Delta_{ec-des}H^\circ(H_{abs})$ as a function of X_H.

respect to the standard potential of the H$^+$/H$_2$ redox couple E°(H$^+$/H$_2$) imply an external H$_2$ fugacity lower than p°, and negative potentials with respect to E°(H$^+$/H$_2$) imply an external H$_2$ fugacity higher than p°. The H$_2$ fugacity refers to the effective pressure of H$_2$ above the electrolyte solution (*27*).

In situ TEM–electron energy loss spectroscopy was used by others to study Pd hydride formation and revealed that, in the case of single cubic Pd-NPs that have side lengths in the range of 13 to 65 nm, the α-to-β phase transition plateau at $T = 246$ K corresponds to H$_2$(g) pressure that is in the range of 10 to 100 Pa (*11*). Although the actual H loading was not measured, the authors performed calculations on the assumption that X_H was in the range of 0.60 to 0.70. Our new results demonstrate that, under electrochemical conditions, the octahedral Pd-NPs can absorb significant amounts of H and values as high as $X_H = 0.90$ can be achieved. In addition, the maximum loading of $X_H = 0.90$ can be reached at lower equivalent pressures than those reported in the literature (*11, 28, 29*). We propose that this unique behavior can be assigned to the octahedral shape of Pd particles and their nanoscopic size. Specifically, (111) facets dominate the entire structure of the octahedral Pd-NPs, although the edges mimic (110) facets but make a small contribution to the overall surface area. Because the surface coordination numbers of fcc(111) and fcc(100) are 9 and 8, respectively, the surface tension of the fcc(111) face is smaller than that of the fcc(100) face. Absorption of H gives rise to an expansion of the Pd lattice, which is opposed by the surface tension. At this stage of our analysis, we propose that, in the case of small octahedral Pd-NPs, the counteracting lattice expansion due to H absorption and lattice compression due to the surface tension create a structure that favors significantly higher H loading than in the case of cubic NPs or bulk Pd materials. The large increase (30 to 50%) in the H loading at lower equivalent H$_2$(g) pressures as compared to other Pd nanomaterials

and bulk materials makes octahedral Pd-NPs very promising materials for possible future applications such as miniaturized H storage devices and metal hydride batteries.

Figure 3C presents $\ln f_{H_2}$ versus $1/T$ plots for $0.10 \leq X_H \leq 0.80$, with an interval of $\Delta X_H = 0.10$ (calculations were performed for an interval of $X_H = 0.05$, but for clarity of presentation, these additional plots are not shown). These relationships are linear (the correlation coefficient is at least 0.98), and their slopes, which are determined through the application of Eq. 2, make the determination of the enthalpy of electrochemical H absorption and H$_{abs}$ desorption [$\Delta_{ec-abs}H^\circ(H_{abs})$ and $\Delta_{ec-des}H^\circ(H_{abs})$] possible.

$$\left(\frac{\partial(\ln\sqrt{f_{H_2}/p^\circ})}{\partial T}\right)_{X_H} = -\frac{\Delta_{ec-abs}H^\circ(H_{abs})}{R\,T^2}$$

and

$$\left(\frac{\partial(\ln\sqrt{f_{H_2}/p^\circ})}{\partial T}\right)_{X_H} = \frac{\Delta_{ec-des}H^\circ(H_{abs})}{R\,T^2} \quad (2)$$

where p° is the standard pressure and R is the ideal gas constant. Figure 3D shows plots of $\Delta_{ec-abs}H^\circ(H_{abs})$ and $\Delta_{ec-des}H^\circ(H_{abs})$ as a function of X_H and demonstrates that $\Delta_{ec-abs}H^\circ(H_{abs})$ adopts values between −19.6 and −29.4 kJ mol^{-1}, whereas $\Delta_{ec-des}H^\circ(H_{abs})$ adopts values between +15.9 and +46.3 kJ mol^{-1}. Because for a given X_H the absolute values of $\Delta_{ec-abs}H^\circ(H_{abs})$ and $\Delta_{ec-des}H^\circ(H_{abs})$ are different, their sum, defined as $\delta\Delta H^\circ(H_{abs}) = \Delta_{ec-ads}H^\circ(H_{abs}) + \Delta_{ec-des}H^\circ(H_{abs})$, is nonzero and adopts

mainly positive values that gradually decrease from the highest value of +18.3 kJ mol^{-1} to the only negative value of −3.7 kJ mol^{-1} for X_H = 0.85 (fig. S7). The mainly positive values of $\delta\Delta H°(H_{abs})$ indicate that the heat absorbed during H_{abs} desorption is greater than the heat released during H absorption. In fig. S6C, the graph presents ln f_{H_2} versus $1/T$ plots for $0.10 \leq X_H \leq 0.65$, with an interval of ΔX_H = 0.05, and in fig. 6D, the graph plots $\Delta_{ec-abs}H°(H_{abs})$ and $\Delta_{ec-des}H°(H_{abs})$ as a function of X_H for cubic Pd-NPs. They demonstrate that $\Delta_{ec-abs}H°(H_{abs})$ adopts values between −12.0 and −5.3 kJ mol^{-1}, whereas $\Delta_{ec-des}H°(H_{abs})$ adopts values between +9.5 and +28.4 kJ mol^{-1}. Although the Pd-H system has been extensively investigated, most of the thermodynamic data refer to bulk materials, and there are few studies dedicated to H absorption in Pd nanomaterials. In situ luminescence probe studies of H absorption in cubic Pd-NPs that have side lengths in the range of 14 to 110 nm resulted in the determination of $\Delta_{abs}H°(H_{abs})$ that varies from −13.7 kJ mol^{-1} for the smallest NPs to −16.4 kJ mol^{-1} for the largest ones (the original data that report enthalpy values per mole of H$_2$ are converted to enthalpy values per 1 mole of H$_{abs}$) (29). Analogous data for H absorption and H$_{abs}$ desorption in bulk Pd materials are $\Delta_{abs}H°(H_{abs})$ = −18.2 kJ mol^{-1} and $\Delta_{des}H°(H_{abs})$ = +20.6 kJ mol^{-1} (30). Our results indicate that, due to the nanoscopic size of the Pd particles and their octahedral shape, H absorption is more exothermic and H$_{abs}$ desorption is more endothermic than in the case of bulk Pd materials or cubic Pd-NPs. Knowledge of the heat evolved during H absorption and H$_{abs}$ desorption is of importance to nanotechnology, where thermal requirements (for example, heat capacity) are needed to take into account in the design of nanoscopic devices. The enthalpy values reported here are very accurate because (i) electrochemical methods offer very precise determination of the amount of adsorbed H (H$_{UPD}$) and absorbed H (H$_{abs}$) by integrating cathodic and anodic CV profiles, (ii) applied potential values can be easily controlled to ±1 mV, and (iii) electrochemical measurements combined with thermodynamic equations facilitate the determination of the enthalpy of H absorption and H$_{abs}$ desorption for a broad range of X_H values.

The entropy of H absorption and H$_{abs}$ desorption [$\Delta_{ec-abs}S°(H_{abs})$ and $\Delta_{ec-des}S°(H_{abs})$] can be determined by applying the van't Hoff equation (Eq. 2) to the results presented in Fig. 3C. The values of $\Delta_{ec-abs}S°(H_{abs})$ are negative and increase almost linearly from −58.7 to −33.9 J mol^{-1} K^{-1} with increasing X_H. The values of $\Delta_{ec-des}S°(H_{abs})$ decrease nonlinearly from +91.9 to +19.5 J mol^{-1} K^{-1} with increasing X_H (fig. S8). Knowledge of the entropy values makes possible the determination of the Gibbs energy of H absorption and H$_{abs}$ desorption [$\Delta_{ec-abs}G°(H_{abs})$ and $\Delta_{ec-des}G°(H_{abs})$], as well as their sum defined as $\delta\Delta G°(H_{abs})$ = $\Delta_{ec-ads}G°(H_{abs})$ + $\Delta_{ec-des}G°(H_{abs})$ as a function of X_H (fig. S9). For the five temperatures, the values of $\Delta_{ec-abs}G°(H_{abs})$ are consistently negative and between −12.0 and −8.3 kJ mol^{-1}, whereas the values of $\Delta_{ec-des}G°(H_{abs})$ are positive and between +14.9 and +9.4 kJ mol^{-1}. For each temperature, the values of $\Delta_{ec-abs}G°(H_{abs})$ increase with increasing X_H, and those of $\Delta_{ec-des}G°(H_{abs})$ decrease with increasing X_H, indicating that the averaged interactions between H$_{abs}$ atoms are repulsive. In the case of $0.10 \leq X_H \leq 0.80$, the $\Delta_{ec-abs}G°(H_{abs})$ versus X_H and $\Delta_{ec-des}G°(H_{abs})$ versus X_H plots are linear, pointing to a Frumkin-like behavior. Finally, the values of $\delta\Delta G°(H_{abs})$, which are a measure of the absorption-desorption hysteresis, are positive and small for the entire range of X_H and all five temperatures. In an important contribution (26), it was proposed that the hysteresis in the f_{H_2} versus X_H plots, which is even observed in the case of single Pd-NPs, arises on the basis of an energetic interplay associated with the formation of dislocations and the coherency strain that develops at the metal/metal hydride interface during the hydride forma-

tion. The size of the plateau can be different in the case of two nominally identical NPs because they can have different dislocations and, consequently, can accommodate lattice strain to a different extent. The nonzero values of $\delta\Delta G°(H_{abs})$ reported above for an ensemble of Pd-NPs are an overall measure of the energetics of dislocation formation and lattice strain accommodation.

Mechanism of H absorption in octahedral Pd-NPs

In Fig. 1D, the CV profile points to a unique behavior of Pd-NPs in the sense that UPD H, H absorption, and HER occur in distinct potential ranges. Because $\Delta_{ec-ads}G°(H_{UPD})$ is more negative than $\Delta_{ec-abs}G°(H_{abs})$, H$_{UPD}$ does not undergo transition to become H$_{abs}$ as in the case of bulk Pd materials (9). Elsewhere (10, 18, 19), it was proposed that in the case of Pt(111) or Rh(111) electrodes, H$_{UPD}$ occupies either the octahedral site (Oh) between the first and the second surface monolayer (ML) or the threefold hollow site right above the Oh site but while still being embedded in the surface lattice; H$_{UPD}$ in this site is referred to as fcc(111)-H$_{UPD(Oh)}$ (fig. S9). If a complete ML of H$_{UPD}$ atoms occupies all the Oh sites, then H absorption can proceed only through the adjacent tetrahedral sites (Td) between the first and second ML of Pd atoms. The adsorbed H atom in the Td site referred to as fcc(111)-H$_{ads(Td)}$ is a short-lived intermediate state due to lateral repulsions; it undergoes transition to become H$_{abs}$ and eventually occupies the vacant interstitial sites beneath the second ML of Pd atoms.

Gas-phase H absorption in Pd materials can be modeled using the surface stress model described elsewhere (30) and can be adapted to Pd-NPs (11). It is based on an assumption that, upon H absorption, Pd-NPs develop a core-shell structure, with each component having its unique H loading. The H intake in the shell is fast, and this region quickly reaches its maximum H loading and only then that H becomes absorbed in the core. The model leads to Eqs. 3 and 4 that relate the overall H loading (X_H) and H loading in the shell ($X_{H,shell}$) to f_{H_2}, T, the NP diameter, and the shell thickness.

$$\frac{RT}{2}\ln\left(\frac{f_{H_2}}{p°}\right) = \Delta H°_{H,\,g\to s} - T\Delta S°_{H,\,g\to s} + RT\ln\left(\frac{X_H}{1-X_H}\right)$$
$$+ \Delta\mu_{H^+}(X_H T) + \Delta\mu_{e^-}(X_H) + \Delta\mu_{H,stress} \quad (3)$$

where

$$\Delta\mu_{H,stress} = \frac{-3KV_H^2(X_{H,shell}-X_H)}{3V_{Pd}+V_H X_H}\frac{2\hat{d}\ (3+3\hat{d}+\hat{d}^2)}{3(1+\hat{d})^3}\frac{1-2\nu}{1-\nu} \quad (4)$$

The variables appearing in these equations and the values of physical parameters required to perform simulations are provided in the Supplementary Materials. The application of this model to our experimental data yields a shell thickness of t = 0.817 nm and a maximum H loading in the shell ($X_{H,shell}$ = 1). The shell thickness of 0.817 nm corresponds to the three atomic layers of Pd. The model does not distinguish between H$_{UPD}$ and H$_{abs}$, because both are in the Pd lattice, and it treats them as H atoms occupying interstitial sites. Bearing in mind the proposal that the H$_{UPD}$ species occupy the octahedral sites beneath the first Pd monolayer (Fig. 4A), the subsequent two layers of H$_{abs}$ occupy the interstitial sites beneath the second and third Pd monolayers (Fig. 4B). The experimentally determined overall maximum H loading of X_H = 0.90 and the
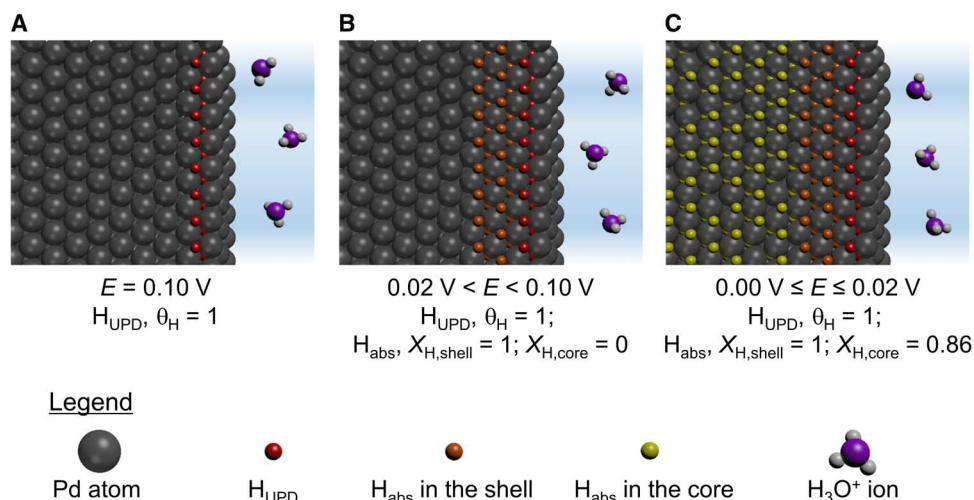
Fig. 4. Visual representation of the different steps of H_{UPD} adsorption and H absorption in octahedral Pd-NPs. (**A**) H_{UPD} species that occupy the octahedral sites beneath the first Pd surface layer. (**B**) H_{abs} beneath the second and third Pd monolayers; H_{UPD}, H_{abs}, and the four topmost Pd layers that together form the shell region. (**C**) H_{abs} in the core of the Pd-NP.
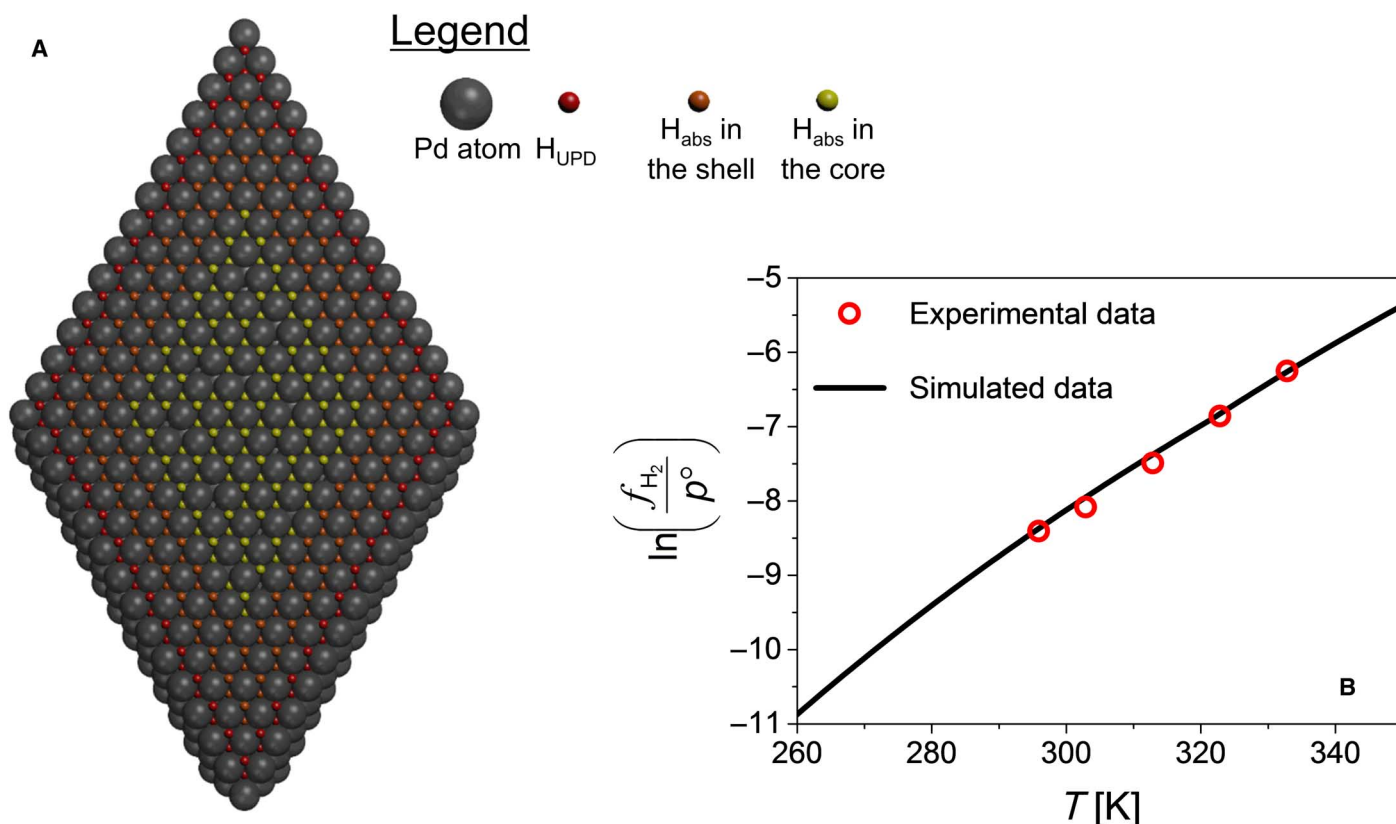
Fig. 5. Surface stress model for H absorption in and H_{abs} desorption from octahedral Pd-NPs. (**A**) Visual representation of the cross section of a single octahedral Pd-NP loaded with H to $X_H = 0.90$ showing H_{UPD} beneath the first Pd layer, H_{abs} in the shell region, and H_{abs} in the NP core. (**B**) Comparison of the calculated $H_2(g)$ fugacity values (black line) to the experimentally determined data (red points) required to reach $X_H = 0.90$.

shell loading of $X_{H,shell} = 1$ together imply that the core loading equals $X_{H,core} = 0.86$ (Fig. 4C). A schematic representation of a single octahedral Pd-NP that has reached a maximum H loading of $X_H = 0.90$ and has a core-shell structure is presented as a cross section in Fig. 5A. The surface stress model can be used to calculate a set of f_{H_2} and T values

required for Pd-NPs to reach the maximum H loading of $X_H = 0.90$. In Fig. 5B, the solid black line presents the calculated values of $\ln\left(\frac{f_{H_2}}{p^\circ}\right)$ as a function of T, whereas the red points refer to our data. The agreement indicates that the surface stress model can be successfully used to model H absorption in small Pd-NPs under electrochemical conditions.

DISCUSSION

In summary, small octahedral Pd-NPs that have an average size of 7.8 nm can be used as H host materials. Under electrochemical conditions at room or elevated temperatures, they can be repetitively charged with H and discharged without any modification to their shape or size. Because of their nanoscopic size, the charging and discharging are quickly achieved, and no residual absorbed H remains in the Pd nano-lattice. Pulverization of bulk H-storing materials is an important technological challenge that limits the life cycle of Ni-M(H) batteries. The lack of any structural changes in the octahedral Pd-NPs upon H absorption and H_{abs} desorption suggests that the degradation (pulverization) of bulk materials is due to the presence of grain boundaries and other structural defects. The octahedral Pd-NPs give rise to a new behavior: the separation of voltammetry features associated with H adsorption, H absorption, and H_2 generation. Together, this property and temperature-dependent experimental research make the analysis of thermodynamic and kinetic parameters of the three processes possible. Electrochemical measurements offer precise control of the applied potential and exact determination of the amount of adsorbed and absorbed H. Consequently, the analysis of electrochemical H adsorption and absorption yields accurate values of thermodynamic state functions. The nanoscopic nature of the Pd particles (a reduced lattice parameter) results in a higher degree of immobilization of electrochemically adsorbed H and a stronger surface bond as compared to bulk H-adsorbing PGMs. Because of the nanoscopic nature of the Pd particles and their octahedral shape that gives rise to predominantly (111) surface orientation of atoms, the absorption of H is more exothermic and the desorption of H_{abs} is more endothermic than in the case of bulk Pd materials or cubic Pd-NPs of similar size. It is an important new piece of information because the performance and lifetime of miniaturized energy-storing devices are related to their heat capacity, and excessive heat evolution can lead to their gradual failure. Although this contribution deals only with octahedral and cubic Pd-NPs of similar size, it is conceivable that a similar analysis could be performed for Pd-NPs of different shapes and dimensions. A systematic experimental approach could result in the identification of a critical dimension and a preferred shape, which, together, give rise to size- and structure-dependent phenomena. The mechanism of electrochemical H absorption in Pd-NPs differs from that observed in the case of bulk materials because the adsorbed H (UPD H) does not undergo transition to become absorbed H. In addition, the external shell of the octahedral Pd-NPs becomes saturated with H, and it is only then that the core starts absorbing H. Upon H absorption, the Pd-NPs develop a unique core-shell-skin structure, where the shell-skin has a maximum H loading of $X_{H,shell-skin} = 1.00$ and the core has an H loading of $X_{H,core} = 0.86$. The overall maximum H loading, which is $X_H = 0.90$, is assigned to the Pd-NP shape and size. This H loading exceeds, by ca. 30 to 50%, the H loading capacity of bulk Pd materials or similar and larger cubic Pd-NPs. The structural integrity of the octahedral Pd-NPs and their exceptionally high H loading capacity make them very promising materials for applications such as miniaturized H storage devices and metal hydride batteries.

MATERIALS AND METHODS

Synthesis of the octahedral Pd-NPs

Octahedral Pd-NPs were synthesized using a method described elsewhere (14). This method was based on chemical reduction of K_2PdCl_4 (17.6 mM) in ultrahigh-purity water using polyvinylpyrrolidone (86 mM) as a surfactant and a mixture of ascorbic acid (85 mM) and citric acid (85 mM) acting as reducing and surface agents.

IL-TEM measurements

IL-TEM measurements were performed using an ultrahigh-resolution JEOL JEM-2100 microscope with a resolution of 0.19 nm. Pd-NPs were placed on a 300-mesh gold grid with a marker for identical position finding. After an IL-TEM image was acquired, the gold grid covered with octahedral Pd-NPs was used as a working electrode in electrochemical experiments. Typically, 10 CV profiles were recorded in the range of $0 \leq E \leq 0.40$ V to observe features for electrochemical H adsorption and absorption (see below). After electrochemical measurements, the gold grid covered with octahedral Pd-NPs was rinsed with ultrahigh-purity water and was transferred to the microscope for post-electrochemical IL-TEM measurements.

Electrochemical measurements

CV experiments were performed in 0.5 M aqueous H_2SO_4 solution outgassed by bubbling ultrahigh-purity $N_2(g)$. They were conducted at a potential scan rate of $s = 1.0$ mV s^{-1} and at different temperatures in the range of $296 \leq T \leq 333$ K. The temperature was controlled using a Haake water bath; the temperature readings inside the cell and the bath agreed to ±0.5 K. The working electrode was a polycrystalline Au disc polished to a mirror-like finish on which 14 µg of unsupported octahedral Pd-NPs was deposited. A glassy carbon plate (surface area of ca. 4 cm^2) was used as a counter electrode. A Pt/Pt black RHE placed in a separate compartment served as a reference electrode. It was connected to the main cell compartment via a Luggin capillary. All potential values were measured and are reported with respect to RHE.

REFERENCES AND NOTES

1. C. Burda, X. Chen, R. Narayanan, M. A. El-Sayed, Chemistry and properties of nanocrystals of different shapes. *Chem. Rev.* **105**, 1025–1102 (2005).
2. C. Bianchini, P. K. Shen, Palladium-based electrocatalysts for alcohol oxidation in half cells and in direct alcohol fuel cells. *Chem. Rev.* **109**, 4183–4206 (2009).
3. V. Polshettiwar, C. Len, A. Fihri, Silica-supported palladium: Sustainable catalysts for cross-coupling reactions. *Coord. Chem. Rev.* **253**, 2599–2626 (2009).
4. F. A. Lewis, *Palladium-Hydrogen System* (Academic Press, 1967).
5. L. Schlapbach, *Hydrogen in Intermetallic Compounds I* (Springer-Verlag, 1988).
6. L. Schlapbach, *Hydrogen in Intermetallic Compounds II* (Springer-Verlag, 1992).
7. R. A. Varin, T. Czujko, Z. S. Wronski, *Nanomaterials for Solid State Hydrogen Storage* (Springer, 2009).
8. G. Jerkiewicz, Electrochemical hydrogen adsorption and absorption. Part 1: Underpotential deposition of hydrogen. *Electrocatalysis* **1**, 179–199 (2010).

9. S. Y. Qian, B. E. Conway, G. Jerkiewicz, Comparative effects of adsorbed S-species on H sorption into Pd from UPD and OPD H: A kinetic analysis. *Int. J. Hydrogen Energy* **25**, 539–550 (2000).

10. A. Zolfaghari, G. Jerkiewicz, Temperature-dependent research on Pt(111) and Pt(100) electrodes in aqueous H_2SO_4. *J. Electroanal. Chem.* **467**, 177–185 (1999).

11. A. Baldi, T. C. Narayan, A. L. Koh, J. A. Dionne, In situ detection of hydrogen-induced phase transitions in individual palladium nanocrystals. *Nat. Mater.* **13**, 1143–1148 (2014).

12. G. Alefeld, J. Völkl, *Hydrogen in Metals I* (Springer-Verlag, 1978).

13. G. Alefeld, J. Völkl, *Hydrogen in Metals II* (Springer-Verlag, 1978).

14. A. Zalineeva, S. Baranton, C. Coutanceau, G. Jerkiewicz, Electrochemical behavior of unsupported shaped palladium nanoparticles. *Langmuir* **31**, 1605–1609 (2015).

15. A. J. Bard, R. Parsons, J. Jordan, *Standard Potentials in Aqueous Solutions* (Marcel Dekker, 1985).

16. A. Zadick, L. Dubau, A. Zalineeva, C. Coutanceau, M. Chatenet, When cubic nanoparticles get spherical: An Identical Location Transmission Electron Microscopy case study with Pd in alkaline media. *Electrochem. Commun.* **48**, 1–4 (2014).

17. M. Baldauf, D. M. Kolb, A hydrogen adsorption and absorption study with ultrathin Pd overlayers on Au(111) and Au(100). *Electrochim. Acta* **38**, 2145–2153 (1993).

18. G. Jerkiewicz, A. Zolfaghari, Comparison of hydrogen electroadsorption from the electrolyte with hydrogen adsorption from the gas phase. *J. Electrochem. Soc.* **143**, 1240–1248 (1996).

19. G. Jerkiewicz, A. Zolfaghari, Determination of the energy of the metal–underpotential-deposited hydrogen bond for rhodium electrodes. *J. Phys. Chem.* **100**, 8454–8461 (1996).

20. J. Solla-Gullón, P. Rodríguez, E. Herrero, A. Aldaz, J. M. Feliu, Surface characterization of platinum electrodes. *Phys. Chem. Chem. Phys.* **10**, 1359–1373 (2008).

21. P. Urchaga, S. Baranton, C. Coutanceau, G. Jerkiewicz, Electro-oxidation of CO_{chem} on Pt nanosurfaces: Solution of the peak multiplicity puzzle. *Langmuir* **28**, 3658–3663 (2012).

22. D. Strmcnik, K. Kodama, D. van der Vliet, J. Greeley, V. R. Stamenkovic, N. M. Markovic, The role of non-covalent interactions in electrocatalytic fuel-cell reactions on platinum. *Nat. Chem.* **1**, 466–472 (2009).

23. M. Osawa, M. Tsushima, H. Mogami, G. Samjeské, A. Yamakata, Structure of water at the electrified platinum–water interface: A study by surface-enhanced infrared absorption spectroscopy. *J. Phys. Chem. C* **112**, 4248–4256 (2008).

24. G. Jerkiewicz, G. Vatankhah, S.-i. Tanaka, J. Lessard, Discovery of the potential of minimum mass for platinum electrodes. *Langmuir* **27**, 4220–4226 (2011).

25. R. Lamber, S. Wetjen, N. I. Jaeger, Size dependence of the lattice parameter of small palladium particles. *Phys. Rev. B* **51**, 10968–10971 (1995).

26. S. Syrenova, C. Wadell, F. A. A. Nugroho, T. A. Gschneidtner, Y. A. Diaz Fernandez, G. Nalin, D. Świtlik, F. Westerlund, T. J. Antosiewicz, V. P. Zhdanov, K. Moth-Poulsen, C. Langhammer, Hydride formation thermodynamics and hysteresis in individual Pd nanocrystals with different size and shape. *Nat. Mater.* **14**, 1236–1244 (2015).

27. G. Jerkiewicz, Hydrogen sorption AT/IN electrodes. *Prog. Surf. Sci.* **57**, 137–186 (1998).

28. G. Li, H. Kobayashi, J. M. Taylor, R. Ikeda, Y. Kubota, K. Kato, M. Takata, T. Yamamoto, S. Toh, S. Matsumura, H. Kitagawa, Hydrogen storage in Pd nanocrystals covered with a metal–organic framework. *Nat. Mater.* **13**, 802–806 (2014).

29. C. Lebouin, Y. Soldo, S. A. Grigoriev, M. Guymont, P. Millet, Kinetics of hydrogen sorption by palladium nanoparticles. *Int. J. Hydrogen Energy* **38**, 966–972 (2013).

30. C. Lemier, J. Weissmüller, Grain boundary segregation, stress and stretch: Effects on hydrogen absorption in nanocrystalline palladium. *Acta Mater.* **55**, 1241–1254 (2007).

31. H. Brodowsky, On the non-ideal solution behavior of hydrogen in metals. *Ber. Bunsenges. Phys. Chem.* **76**, 740–746 (1972).

32. J. D. Clewley, T. Curran, T. B. Flanagan, W. A. Oates, Thermodynamic properties of hydrogen and deuterium dissolved in palladium at low concentrations over a wide temperature range. *J. Chem. Soc. Faraday Trans. 1* **69**, 449–458 (1973).

Science Advances

Octahedral palladium nanoparticles as excellent hosts for electrochemically adsorbed and absorbed hydrogen

Anna Zalineeva, Stève Baranton, Christophe Coutanceau and Gregory Jerkiewicz

ARTICLE TOOLS	http://advances.sciencemag.org/content/3/2/e1600542
SUPPLEMENTARY MATERIALS	http://advances.sciencemag.org/content/suppl/2017/01/30/3.2.e1600542.DC1
REFERENCES	This article cites 25 articles, 1 of which you can access for free http://advances.sciencemag.org/content/3/2/e1600542#BIBL
PERMISSIONS	http://www.sciencemag.org/help/reprints-and-permissions

Use of this article is subject to the Terms of Service